Mechanical Design of Rotors for Permanent Magnet High Speed Electric Motors for Turbocharger Applications

Simon M Barrans[1]*, Mahir M J Al-Ani [1], Jeff Carter[2]

[1] Turbocharger Research Institute, University of Huddersfield, Huddersfield, United Kingdom
[2] BorgWarner Turbo Systems, Bradford, United Kingdom
*s.m.barrans@hud.ac.uk

Abstract: Realization of electrically boosted turbochargers requires electric motors capable of operating at very high speeds. These motors often use a permanent magnet rotor with the magnets retained within an interference fit external sleeve. Whilst it is possible to model such systems numerically, these models are an inefficient tool for design optimization. Current analytical models of rotors typically consider the stresses induced by the shrink fit of the sleeve separately from the stresses generated by centripetal forces due to rotation. However, such an approach ignores the frictional interaction between the components in the axial direction. This paper presents an analytical model that simultaneously accounts for interaction between the magnet and outer sleeve in both the radial and axial directions at designed interference and with the assembly subjected to centripetal and thermal loads. Numerical models presented show that with only moderate coefficients of friction and rotor lengths; axial load transfer between magnet and sleeve takes place over a short distance at the ends of the assembly. The paper then demonstrates how the analytical model aids definition of a feasible set of rotor designs and selection of an optimum design.

1. Introduction

Arsie et al. [1] have investigated the benefit of coupling an electric motor/generator to a turbocharger in terms of fuel consumption reduction. As they state, such systems have not yet been widely implemented on light-duty automotive engines. One reason for this is the challenge in manufacturing an electric machine able to operate in the 100 to 300 krpm range needed for smaller turbochargers whilst keeping the machine small enough not to interfere with other elements of the engine system. Keller et al [2] had emissions reduction as the motivation for introducing an electric machine into the air induction circuit. In their work a range of electric machine options are considered and it is concluded that a synchronous machine with a permanent magnet (PM) rotor will be the most efficient and power dense. In addition to applications in turbocharging, Gerada et al [3] highlight an increasing demand for high speed electrical machines in flywheel energy storage, high speed spindles, and a number of other areas.

The construction of PM rotors is divided into two types according to the method used to attach the magnets to the rotor. Interior mounted permanent magnetic (IPM) rotors have discrete magnets embedded within the iron core of the rotor whereas surface-mounted permanent magnet (SPM) rotors have the magnets glued to the outer surface of the rotor. SPM rotors will normally have an outer retaining ring or sleeve around the magnets (see for example Binder et al [4]). Some references [5] criticize SPM's as the sleeve, which must be of a non-magnetic material, effectively increases the electromagnetic air gap between rotor and stator and hence reduces motor efficiency. However a number of references [6], [4] and [7] observe that due to the stresses generated due to rotation, only SPM rotors are appropriate for high speed applications. Indeed , as Gieras [7] observes, 'interior-type PM rotors without retaining sleeves can be used at speeds not exceeding 6000 rpm' and Zhang et al [8] observe that a retaining sleeve may still be used for IPM rotors. Rare earth magnets such as samarium cobalt SmCo (SmCo5 or Sm2Co17) or neodymium (Nd2Fe14B) are often used in SPM rotors. These materials are formed from sintering or bonding and are typically very weak in tension. It is important therefore that they are held in compression as the rotor speed increases.

As [6], [9] and [10] have noted, as the operating speed of the electric machine increases, the mechanical design of the rotor becomes the critical factor rather than the electromagnetic design. A number of authors have addressed the mechanical design. In some cases [11], [12], [13] and [14] finite element analysis (FEA) has been used as the principal stress analysis tool. In the latter case the rotor being designed was for a large electric machine (rotor diameter 686 mm) and was a complex assembly of parts so there was no alternative but to use FEA. Other SPM rotors are much simpler designs and a number of researchers have proposed carrying out the mechanical design using classical methods. Wang et al [15] have analyzed the permanent magnet and the outer sleeve as a pair of interfering cylinders, as illustrated in figure 1. In this figure the two cylinders are shown with a common radius, , which will be the assembled state. However, prior to assembly, the magnet has a larger outer radius, , and the sleeve has a smaller radius, . This interference between the cylinders is essential to ensure that the magnet remains in compression in the circumferential direction. The cylinders analyzed in [15] are long and would therefore generally be analyzed as being in generalized plane strain (see for example [16] (page 536)). Whilst the state of stress and strain assumed in [15] is not stated, it is apparent from the equations presented that plane stress has been assumed. In [15] it is observed that the change in interference due to rotational effects must be accounted for. The impact of this change in interference does not appear to have been accounted for in the analysis presented in [4]. Zhang et al [17] use a plane stress model to determine the

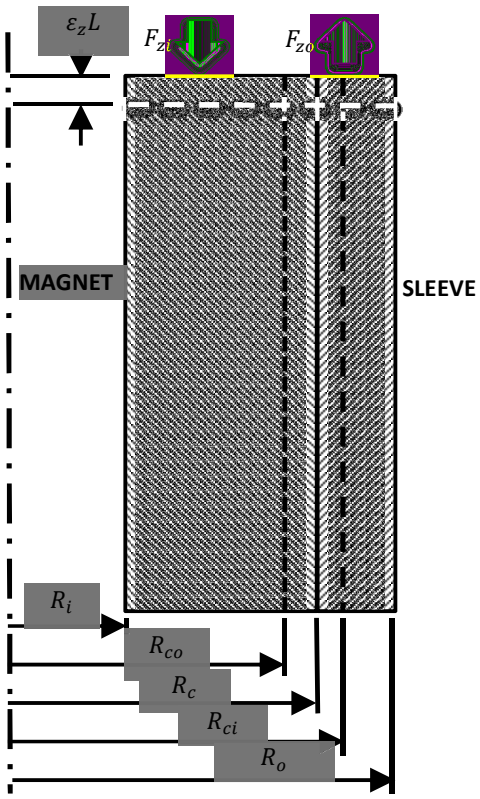

Fig. 1. *Simple rotor assembly (axisymmetric section)*

stresses in a rotor assembly with a carbon fibre and state that axial strain is neglected. Other papers in this area such as [18] refer to [15] for the analytical work or in the case of [11] the theory presented in [4] is used. Yon et al [19] did not use the classical compound cylinder theory, as the magnets in their rotor were segmented and separated circumferentially by substantial layers of other material. In common with other researchers in the field, the theory presented in the current paper assumes that separation layers between the magnets are thin enough to be ignored and that the magnets will always be held in compression.

As Smith et al [6] have noted, there will be axial load transfer between the magnet and the sleeve. However, the existing analytical methods for analyzing rotor assemblies do not account for this. Even in [6] it is assumed that the components are in plane stress (i.e. no axial load) and that only a shear stress is generated in the axial direction. In this paper an alternate analysis of SPM rotors will be presented which accounts for axial load transfer between the magnets and sleeve at all stages of operation.

2. Theoretical analysis

2.1. Classical Models

As indicated above the common approach used in determining the stress in SPM rotors is to consider the analysis in two steps:

- Determine the stresses and circumferential expansion of the cylinders as unconnected parts, due to centripetal and thermal loads.
- Based on the deformed geometry found in the first step, determine the stresses due to the interference between the cylinders.

The total stress in the radial and circumferential directions can then be found as the arithmetic sum of the stresses due to rotation and shrinkage.

In determining the stresses due to centripetal loads, two approaches may be taken: assuming plane stress (PS) or assuming generalized plane strain (GPS). Both approaches are described in text books on stress analysis such as [16]. For the GPS case it is assumed that on a given cross section perpendicular to the axis, the axial strain is constant.

The radial, $\sigma_{r,\omega}$, and circumferential, $\sigma_{\theta,\omega}$, stresses at a radius are given by:

$$\sigma_{r,\omega} = A - \frac{B}{r^2} - \frac{3-2\nu}{8(1-\nu)}\rho\omega^2 r^2 \qquad (1)$$

$$\sigma_{\theta,\omega} = A + \frac{B}{r^2} - \frac{1+2\nu}{8(1-\nu)}\rho\omega^2 r^2 \qquad (2)$$

Where A and B are constants dependent on the boundary conditions, ν and ρ are the Poisson's ratio and density of the material respectively and ω is the speed of rotation. If it is assumed that there is no interaction between the cylinder and its surroundings at both the inner, R_1, and outer, R_2, radii, (i.e. zero radial stress at these points) these equations become:

$$\sigma_{r,\omega} = \frac{3-2\nu}{8(1-\nu)}\rho\omega^2\left\{R_2^2 + R_1^2 - \frac{R_2^2 R_1^2}{r^2} - r^2\right\} \qquad (3)$$

$$\sigma_{\theta,\omega} = \frac{\rho\omega^2}{8(1-\nu)}\left\{(3-2\nu)\left(R_2^2 + R_1^2 + \frac{R_2^2 R_1^2}{r^2}\right) - (1+2\nu)r^2\right\} \qquad (4)$$

It should be noted that the radii R_1 and R_2 refer to a generic, single cylinder and should not be confused with the dimensions shown in figure 1 for the rotor assembly.

The axial stress in the cylinder can be determined using the condition of generalized plane strain combined with the fact that there is no overall axial load on the cylinder. For the case of generalized plane strain, the axial strain, ε_z is constant through the cylinder wall. Hence:

$$\frac{d\varepsilon_z}{dr} = 0$$

Also, from Hooke's law: $\varepsilon_z = \frac{1}{E}(\sigma_z - \nu(\sigma_\theta + \sigma_r))$

The internal axial load, F_z, generated by the axial stress can be determined from:

$$F_z = \int_{R_1}^{R_2} 2\pi r \sigma_z dr$$

As the internal axial load must be zero, this then gives:

$$\sigma_z = \frac{\nu\rho\omega^2}{4(1-\nu)}(R_2^2 + R_1^2 - 2r^2) \qquad (5)$$

If plane stress is assumed during the rotation step the radial and circumferential stresses are given by:

$$\sigma_{r,\omega} = A - \frac{B}{r^2} - \frac{(3+\nu)}{8}\rho\omega^2 r^2 \quad (6)$$

$$\sigma_{\theta,\omega} = A + \frac{B}{r^2} - \frac{1+3\nu}{8}\rho\omega^2 r^2 \quad (7)$$

Again, the typical approach used to determine the constants A and B is to assume no interaction between the cylinder and its surroundings at the inner and outer radii. In this specific case the equations become:

$$\sigma_{r,\omega} = \frac{3+\nu}{8}\rho\omega^2\left\{R_2^2 + R_1^2 - \frac{R_2^2 R_1^2}{r^2} - r^2\right\} \quad (8)$$

$$\sigma_{\theta,\omega} = \frac{\rho\omega^2}{8}\left\{(3+\nu)\left(R_2^2 + R_1^2 + \frac{R_2^2 R_1^2}{r^2}\right) - (1+3\nu)r^2\right\} \quad (9)$$

And by definition, $\sigma_z = 0$.

For both generalized plane strain and plane stress cases, the circumferential strain, ε_θ, is related to the stresses by Hooke's law:

$$\varepsilon_\theta = \frac{\Delta R}{R} = \frac{1}{E}(\sigma_\theta - \nu\sigma_r - \nu\sigma_z) + \Delta T\alpha \quad (10)$$

Where ΔR is the change in radius, R is the radius, σ_z is the axial stress in the cylinder, ΔT is the change in temperature of the cylinder and α is the coefficient of thermal expansion. It is assumed here that on a given axial section, the temperature of the rotor is uniform. As Li et al [20] determined, the thermal barrier resisting heat transfer from the outer surface of the rotor to the air gap is much larger than the thermal resistance within the rotor components. Hence, temperatures are essentially uniform with respect to radius and vary only slightly along the axis.

Once the changes in dimensions of the cylinders are known, the stress resulting from the interference between them can be calculated. In order to determine these stresses the change in radius of the inner and outer cylinders must be such that they have a matching common radius, R_c, as shown in figure 1. This condition can be expressed as:

$$R_{ci\omega}(1 + \varepsilon_{\theta ics}) = R_{co\omega}(1 + \varepsilon_{\theta ocs}) \quad (11)$$

Where $R_{ci\omega}$ is the outer radius of the inner cylinder at the operating speed, $R_{co\omega}$ is the inner radius of the outer cylinder at the operating speed if the two cylinders are considered as separate entities. $\varepsilon_{\theta ics}$ is the circumferential strain at the outer radius of the inner cylinder generated by the shrinkage pressure, S and $\varepsilon_{\theta ocs}$ is the circumferential strain at the inner radius of the outer cylinder due to S. The shrinkage pressure is the load acting between the two cylinders causing them to deform to become compatible.

The stresses due to S can be determined using the standard Lamé equations as:

$$\sigma_{ri} = \frac{SR_c^2}{R_i^2 - R_c^2}\left(1 - \frac{R_i^2}{r^2}\right) \quad (12)$$

$$\sigma_{\theta i} = \frac{SR_c^2}{R_i^2 - R_c^2}\left(1 + \frac{R_i^2}{r^2}\right) \quad (13)$$

$$\sigma_{ro} = \frac{SR_c^2}{R_o^2 - R_c^2}\left(1 - \frac{R_o^2}{r^2}\right) \quad (14)$$

$$\sigma_{\theta o} = \frac{SR_c^2}{R_o^2 - R_c^2}\left(1 + \frac{R_o^2}{r^2}\right) \quad (15)$$

During the shrinkage analysis, the axial stress is zero for both the plane stress and generalized plane strain cases as there are no end conditions on the cylinders.

Substituting equations (12) to (15) into equation (10) will generate equations for $\varepsilon_{\theta ics}$ and $\varepsilon_{\theta ocs}$. Then, using equation (11), the relationship between the shrinkage pressure and the geometry of the cylinders during rotation can be determined:

$$S = \frac{R_{ci\omega} - R_{co\omega} + \Delta T[R_{ci\omega}\alpha_i - R_{co\omega}\alpha_o]}{\frac{R_{co\omega}\{R_o^2(1+\nu_o) + R_c^2(1-\nu_o)\}}{E_o(R_o^2 - R_c^2)} + \frac{R_{ci\omega}\{R_c^2(1-\nu_i) + R_i^2(1+\nu_i)\}}{E_i(R_c^2 - R_i^2)}} \quad (16)$$

The stress at any point in either the magnets or the sleeve can then be calculated using equations (12) to (15).

2.2. New Model

The two analysis approaches described above assume that there is no axial load transfer between the magnet and the sleeve. However, friction will be present at the interface between these parts and this will place restrictions on the axial deformation. Assuming that there is sufficient friction present to lock the two cylinders together, there are two equilibrium and two compatibility conditions on the system:

A. In the radial direction there must be force equilibrium at the interface between the cylinders. This is expressed as a shrinkage pressure, S.

B. There must be equilibrium of forces in the axial direction between the two cylinders:

$$F_{zi} = -F_{zo} \quad (17)$$

Where F_{zi} and F_{zo} are the axial forces in the inner and outer cylinders respectively (see figure 1).

C. At the interface there must be circumferential strain compatibility. This can be expressed as:

$$R_{ci}(1 + \varepsilon_{\theta ic}) = R_{co}(1 + \varepsilon_{\theta oc}) \quad (18)$$

D. There must be axial strain compatibility (i.e. the cylinders must change in length by the same amount):

$$\varepsilon_{zi} = \varepsilon_{zo} \quad (19)$$

Where ε_{zi} and ε_{zo} are the axial strains in the inner and outer cylinders respectively.

As the cylinders are twice as long as their diameter, away from the free ends, they will be in a state of generalized plane strain. Equations (1) and (2) are therefore applicable. In the previous analyses, during the shrinkage step, there was no axial stress present. This allowed the stresses due to shrinkage to be determined independently of the stresses due to rotation. However, conditions B and D above remove this independence between the stress states. The constants in equations (1) and (2) must therefore be found accounting for both rotation and interference. For the inner cylinder:

At $r = R_i$; $\sigma_{rii} = 0$
$r = R_c$; $\sigma_{ric} = -S$

Where σ_{rii} and σ_{ric} are the radial stresses in the inner cylinder at the bore and the common radius respectively. Substituting the constants found, the stress equations become:

$$\sigma_{ri} = \frac{SR_c^2}{(R_i^2 - R_c^2)}\left(1 - \frac{R_i^2}{r^2}\right) + \frac{3 - 2\nu_i}{8(1-\nu_i)}\rho_i\omega^2 \left\{R_c^2 + R_i^2 - \frac{R_c^2 R_i^2}{r^2} - r^2\right\} \quad (20)$$

$$\sigma_{\theta i} = \frac{SR_c^2}{(R_i^2 - R_c^2)}\left(1 + \frac{R_i^2}{r^2}\right) + \frac{\rho_i\omega^2}{8(1-\nu_i)} \left\{(3 - 2\nu_i)\left(R_c^2 + R_i^2 + \frac{R_c^2 R_i^2}{r^2}\right) - (1 + 2\nu_i)r^2\right\} \quad (21)$$

Considering radial equilibrium, strain compatibility and the condition of generalized plane strain, the axial stress is determined from:

$$\sigma_{zi} = \frac{F_{zi}}{\pi(R_c^2 - R_i^2)} + \frac{\nu_i\rho_i\omega^2}{4(1-\nu_i)}(R_c^2 + R_i^2 - 2r^2) \quad (22)$$

And the axial strain is given by:

$$\varepsilon_{zi} = \frac{1}{E_i}\left(\frac{F_{zi}}{\pi(R_c^2 - R_i^2)} - \frac{2S\nu_i R_c^2}{(R_i^2 - R_c^2)} - \frac{\nu_i\rho_i\omega^2(R_c^2 + R_i^2)}{2}\right) + \Delta T\alpha_i \quad (23)$$

For the outer cylinder the boundary conditions are:

At $r = R_c$; $\sigma_{roc} = -S$
$r = R_o$; $\sigma_{roo} = 0$

Where σ_{roc} and σ_{roo} are the radial stresses in the outer cylinder at the common radius and the outer radius respectively. This leads to:

$$\sigma_{ro} = \frac{SR_c^2}{(R_o^2 - R_c^2)}\left(1 - \frac{R_o^2}{r^2}\right) + \frac{3 - 2\nu_o}{8(1-\nu_o)}\rho_o\omega^2 \left\{R_c^2 + R_o^2 - \frac{R_c^2 R_o^2}{r^2} - r^2\right\} \quad (24)$$

$$\sigma_{\theta o} = \frac{SR_c^2}{(R_i^2 - R_c^2)}\left(1 - \frac{R_o^2}{r^2}\right) + \frac{\rho_o\omega^2}{8(1-\nu_i)} \left\{(3 - 2\nu_o)\left(R_c^2 + R_o^2 + \frac{R_c^2 R_o^2}{r^2}\right) - (1 + 2\nu_o)r^2\right\} \quad (25)$$

In the axial direction:

$$\sigma_{zo} = \frac{F_{zo}}{\pi(R_o^2 - R_c^2)} + \frac{\nu_o\rho_o\omega^2}{4(1-\nu_o)}(R_c^2 + R_o^2 - 2r^2) \quad (26)$$

$$\varepsilon_{zo} = \frac{1}{E_o}\left(\frac{F_{zo}}{\pi(R_o^2 - R_c^2)} - \frac{2S\nu_o R_c^2}{(R_o^2 - R_c^2)} - \frac{\nu_o\rho_o\omega^2(R_c^2 + R_o^2)}{2}\right) + \Delta T_o \quad (27)$$

Determining the stresses and strains at R_c from equations (20) to (27) along with equation (10) and enforcing conditions A to D allows the axial force and shrinkage pressure to be determined from:

$$\begin{bmatrix} U & V \\ X & Y \end{bmatrix}\begin{bmatrix} F_{zo} \\ S \end{bmatrix} = \begin{bmatrix} W \\ Z \end{bmatrix} \quad (28)$$

Where:

$$U = \frac{1}{\pi}[E_i(R_i^2 - R_c^2) - E_o(R_o^2 - R_c^2)]$$

$$V = -2R_c^2[\nu_O E_i(R_i^2 - R_c^2) - \nu_i E_o(R_o^2 - R_c^2)]$$

$$W = (R_o^2 - R_c^2)(R_i^2 - R_c^2)\left\{\frac{\omega^2}{2}[\nu_O E_i\rho_o(R_c^2 + R_o^2) - \nu_i E_o\rho_i(R_c^2 + R_i^2)] + \Delta T(\alpha_i - \alpha_o)E_o E_i\right\}$$

$$X = \frac{1}{\pi}[\nu_i E_o R_{ci}(R_o^2 - R_c^2) + \nu_o E_i R_{co}(R_c^2 - R_i^2)]$$

$$Y = -\{E_o R_{ci}(R_o^2 - R_c^2)[R_c^2(1 - \nu_i) + R_i^2(1 + \nu_i)] + R_{co}E_i(R_c^2 - R_i^2)[R_o^2(1 + \nu_o) + R_c^2(1 - \nu_o)]\}$$

$$Z = (R_c^2 - R_i^2)(R_o^2 - R_c^2)\{E_o E_i[R_{co} - R_{ci} + \Delta T(\alpha_o R_{co} - \alpha_i R_{ci})] + \frac{\rho_o R_{co}\omega^2 E_i}{8(1-\nu_o)}[2(R_c^2 + 3R_o^2) - 4\nu_o(R_o^2 + R_c^2) - 2\nu_o^2(R_o^2 - R_c^2)] - \frac{\rho_i R_{ci}\omega^2 E_o}{8(1-\nu_i)}[2(R_c^2 + 3R_i^2) - 4\nu_i(R_c^2 + R_i^2) - 2\nu_i^2(R_i^2 - R_c^2)]\}$$

Equation (28) can be used to determine the shrinkage pressure and axial force in the cylinders at any rotational speed (including no rotation) and with any change in temperature. Once these terms are found, the radial, circumferential and axial stresses at any point in the cylinders can be determined using equations (12) to (15), (22) and (26).

The von Mises equivalent stress, σ_{VM}, predicted by any of the analysis methods can be determined using:

$$\sigma_{VM} = \sqrt{\frac{1}{2}\{(\sigma_r - \sigma_\theta)^2 + (\sigma_\theta - \sigma_z)^2 + (\sigma_z - \sigma_r)^2\}} \quad (29)$$

Considering an example magnet and sleeve assembly with the parameters shown in Table 1, the three different analysis methods give the results shown in Table 2 with the assembly subjected to no temperature change and a maximum rotational speed of 100,000 rpm. Whilst the three analysis methods give very similar results for the von Mises stress during rotation, the circumferential stresses in the sleeve predicted by the new model are 6.8% higher. These stresses will be critical as they may lead to fatigue cracking. Also, both at rest and at speed, the classical models underestimate the magnitude of the compressive

Table 1. Example rotor parameters

Magnet properties		Sleeve properties	
R_i (mm)	6.349	R_o (mm)	13
R_{ci} (mm)	11.38	R_{co} (mm)	11.35
E_i (GN/m^2)	150	E_o (GN/m^2)	205
ν_i	0.27	ν_o	0.284
ρ_i (kg/m^3)	8400	ρ_o (kg/m^3)	8220
α_i	1×10^{-5}	α_o	1.3×10^{-5}

Table 2 Example rotor stresses (MPa)

State	Stress component	Model PS	Model GPS	Model New model
At rest	$\sigma_{\theta ii}$	-158.7	-158.7	-174.4
	$\sigma_{\theta ic}$	-104.2	-104.2	-114.6
	$\sigma_{\theta oc}$	404.1	404.1	439.4
	σ_{VMoc}	433.9	433.9	440.5
At speed	$\sigma_{\theta ii}$	-33.0	-31.0	-45.8
	$\sigma_{\theta ic}$	-37.8	-39.8	-49.5
	$\sigma_{\theta oc}$	494.2	495.2	528.0
	σ_{VMoc}	519.3	518.8	520.6

circumferential stress in the magnet. At rest, this may lead to failure under compression of the magnet. Under rotation, the classical models would predict this stress becoming tensile (typically the critical state) at a lower speed than the new model. Hence, the maximum permissible operating speed would be underestimated (or the interference could be relaxed to achieve a required operating speed).

3. Finite element model

To test the validity of the new model, a finite element model of an example magnet and sleeve assembly was constructed in the ABAQUS package. It was assumed that the rotor behavior would axisymmetric. This condition will be true whilst a compressive stress is maintained in the circumferential direction within the magnets. The magnets and sleeve had the material and dimensional parameters given in table 1. The interference between the magnets and sleeve was modelled by constructing the parts in their free state and defining surface to surface, small sliding contact at the interface. In the normal direction the 'hard' contact algorithm was specified to ensure that the interference was precisely modelled. The rotor length was specified as 200 mm. While this length is excessive for turbocharger applications, it was used to assess effects of friction in the axial direction.

At the interference, two tangential contact conditions were specified: fully bonded (no sliding) and coulomb friction enforced by Lagrange multipliers. In this section the fully bonded contact condition is considered. The model was subjected to a sequence of four load steps:

1. Interference at ambient temperature.
2. Maximum rotational speed and ambient temperature.
3. Maximum rotational speed and temperature elevated by 200°C.
4. Interference with temperature elevated by 200°C.

To ensure that the interference effect was being correctly modelled a mesh convergence study was carried out with the number of elements through the thickness of both magnets and sleeve being increased. The results of this are shown in figure 2(a). Mesh refinement was then supplemented with mesh biasing to make the elements on the inner and outer radii of both components up to 10 times smaller than those in the center. This further improved the stress convergence, as shown in figure 2(b). In these figures, the mesh with 24 elements through the thickness and a bias

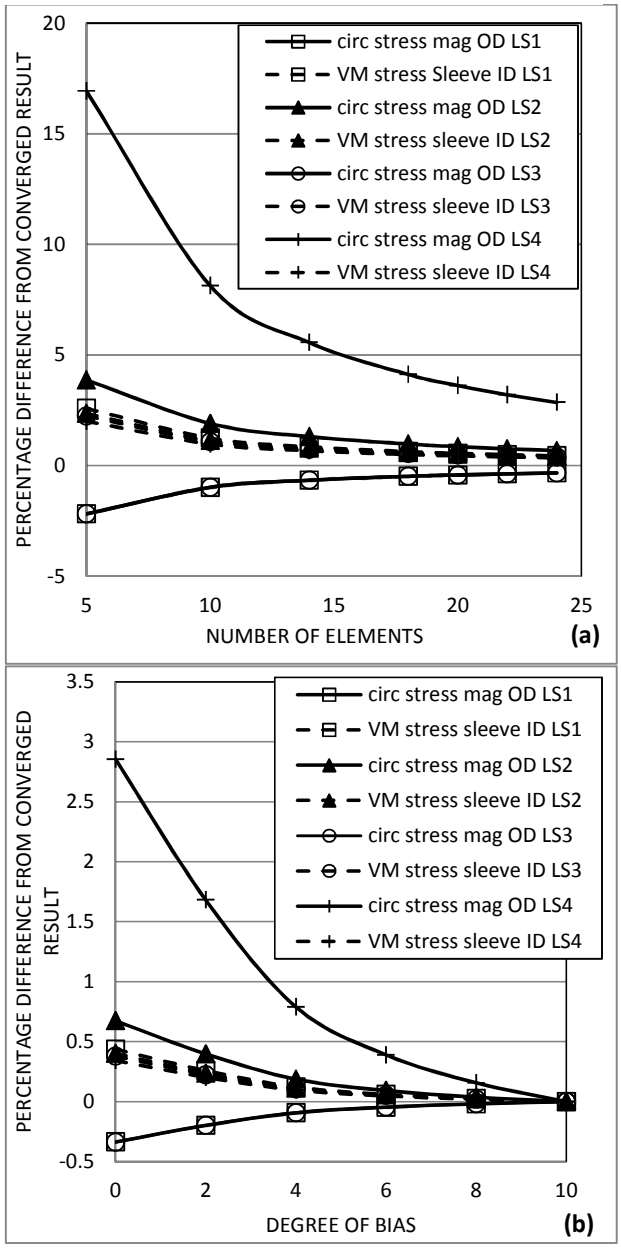

Fig. 2. Mesh convergence study (a) reduction in element size, (b) increasing bias

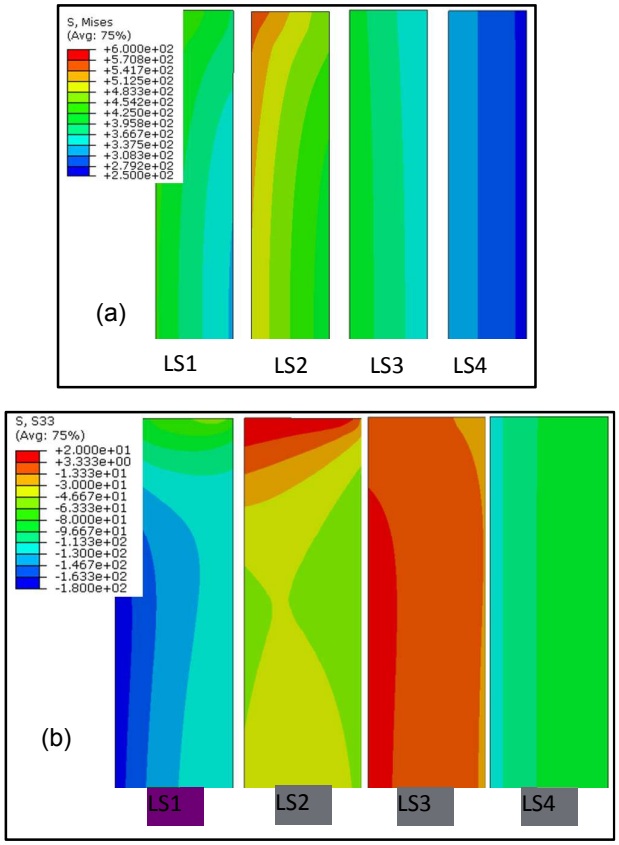

Fig. 3. *(a) von Mises stress in the sleeve, (b) circumferential stress in the magnet*

of 10 is the reference. Steady convergence towards this result can be seen for the two critical results, circumferential stress at the outer diameter of the magnet and von Mises stress at the bore of the sleeve. For all four load-steps, the results have converged to within ±0.2%. This study was carried out for the fully bonded contact condition.

Figure 3 shows the stresses predicted by the finite element model for each load step. In this figure, only the free end of the magnet and sleeve are shown as this is where a variation in the stress distribution occurs. This variation is because the state of strain at this free end switches from generalized plane strain to three-dimensional strain. Likewise, the state of stress switches from being three dimensional in the bulk of each cylinder to plane stress at the free end.

Table 3 compares results obtained from the new theoretical model with those from the bonded interface FEA model on the plane of axial symmetry (i.e. away from any end effect). Good agreement between the new theory and the FEA model is noted across all the results with the difference only going above 1% where the absolute value is small.

4. Friction effect

The new theory assumes that the cylinders are locked together in the longitudinal direction (i.e. the coefficient of friction is infinite). Since this is unrealistic, a study was carried out to determine the impact of friction. This study used the finite element model described in section 3 but with the coulomb friction model replacing the fully bonded contact condition. This contact model allows surfaces to slide past each other once the tangential force applied exceeds the frictional resistance due to the normal force. Prior to slip the tangential force generates shear stresses in the contacting surfaces. The degree of slip between the surfaces and the shear stress are results generated by the FEA package.

Figure 4 shows the amount of slip and the shear stress acting between the sleeve and the magnets at the interface during the rotation step. On the plane of axial symmetry, there is no slip or shear stress. At the free end of the assembly, both slip and shear stress are present. The shear stress reaches a peak some distance into the assembly and then drops off exponentially. At the maximum shear stress point, the amount of slip is zero. This effect is a result of the frictional shear transferring the axial load between the magnet and the sleeve in order to maintain equilibrium between the parts, as assumed in the development of the theory. Once this load transfer has taken place, the parts behave as if locked together. This validates the assumption of axial strain compatibility used in the theory.

The circumferential stresses generated in the magnet and the sleeve at the interference due to shrink fitting alone, are shown in figure 5. It should be noted here that the results for and are almost identical. Again, the amount of friction does not affect the stresses generated once the axial load transfer between the sleeve and the magnets is completed. Two end effects are present in the results. At a point approximately 10 mm from the free end, the stress in the

Table 3 Comparison of new theory to FEA

Load step	Stress component					
	$\sigma_{\theta ii}$	$\sigma_{\theta ic}$	$\sigma_{\theta oc}$	$\sigma_{\theta oo}$	σ_{zoc}	σ_{VMoc}
1 FEA	-171.31	-112.89	439.87	381.10	106.23	440.17
1 Theory	-171.25	-112.35	440.86	381.95	106.44	440.98
1 % diff	-0.04	-0.49	0.23	0.23	0.20	0.18
2 FEA	-42.73	-47.63	528.28	452.28	101.43	520.22
2 Theory	-42.42	-47.40	529.24	453.08	101.68	521.02
2 % diff	-0.72	-0.48	0.18	0.18	0.24	0.15
3 FEA	6.67	-15.08	401.00	342.40	-5.33	421.94
3 Theory	6.95	-15.01	402.13	342.96	-5.28	422.56
3 % diff	4.31	-0.48	0.28	0.16	-0.86	0.15
4 FEA	-121.98	-80.34	313.04	271.22	-0.53	336.23
4 Theory	-121.87	-79.95	313.75	271.83	-0.51	336.88
4 % diff	-0.09	-0.49	0.23	0.23	-2.68	0.19

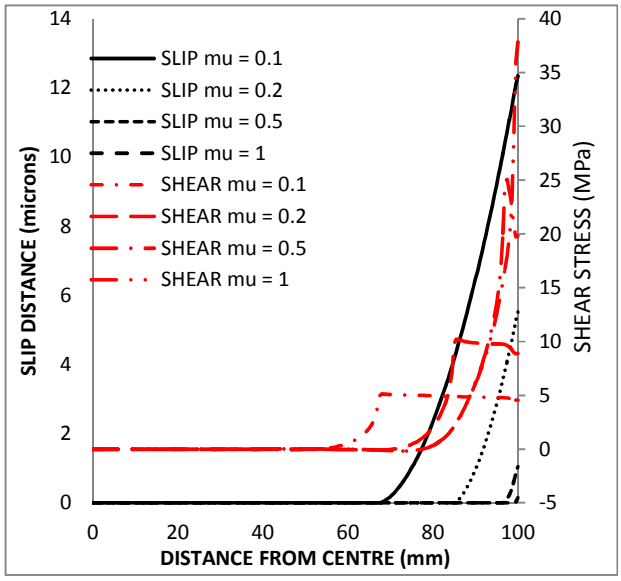

Fig. 4. *Contact interface slip and shear for a range of coefficients of friction (during rotation)*

sleeve drops to a minimum value. This end effect is not dependent on the coefficient of friction but is due to material at the end no longer being constrained to be in a state of generalized plane strain. The new theoretical model does not consider this.

Moving further away from the free end, the effect of load transfer due to friction is observed.

5. Optimization

In the sections above, a rotor design has been shown with a relatively thin walled sleeve and a large interference between sleeve and magnet. This design generated compressive circumferential stresses in the magnet both at rest and during rotation at ambient temperature. However, at the elevated temperature the circumferential stress at the bore of the magnet became tensile under rotation. For typical rare earth magnet materials, these tensile stresses would lead to failure. Hence, this design is not feasible. When evaluating the feasibility of rotor designs, ten design constraints are used:

$$|\sigma_{\theta ii}| \leq |\sigma_{UCS,mag}| \text{ at } \omega = 0 \text{ for } T = T_{amb} \quad (30)$$

$$|\sigma_{\theta ii}| \leq |\sigma_{UCS,mag}| \text{ at } \omega = 0 \text{ for } T = T_{max} \quad (31)$$

$$\sigma_{\theta ic} \leq 0 \text{ at } \omega = \omega_{max} \text{ for } T = T_{amb} \quad (32)$$

$$\sigma_{\theta ic} \leq 0 \text{ at } \omega = \omega_{max} \text{ for } T = T_{max} \quad (33)$$

$$\sigma_{\theta ii} \leq 0 \text{ at } \omega = \omega_{max} \text{ for } T = T_{amb} \quad (34)$$

$$\sigma_{\theta ii} \leq 0 \text{ at } \omega = \omega_{max} \text{ for } T = T_{max} \quad (35)$$

$$\sigma_{VMoc} \leq \sigma_{allow,sleeve} \text{ at } \omega = 0 \text{ for } T = T_{amb} \quad (36)$$

$$\sigma_{VMoc} \leq \sigma_{allow,sleeve} \text{ at } \omega = 0 \text{ for } T = T_{max} \quad (37)$$

$$\sigma_{VMoc} \leq \sigma_{allow,sleeve} \text{ at } \omega = \omega_{max} \text{ for } T = T_{amb} \quad (38)$$

$$\sigma_{VMoc} \leq \sigma_{allow,sleeve} \text{ at } \omega = \omega_{max} \text{ for } T = T_{max} \quad (39)$$

Constraints 30 and 31 ensure that the magnet will not be crushed due to the interference with the sleeve. This

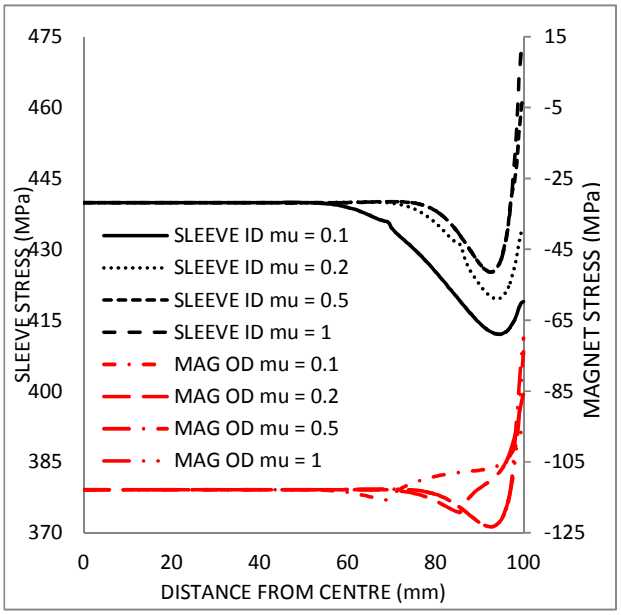

Fig. 5. *Contact interface slip and shear for a range of coefficients of friction (during rotation)*

could occur at either ambient temperature or elevated temperature dependent on the relative coefficients of thermal expansion. In many applications, including turbochargers, the rotor could be at rest at the maximum temperature once the system has warmed up. Constraints 32 to 35 are required to prevent the magnet failing due to tensile circumferential stresses. Constraints 36 to 39 ensure that the sleeve does not yield. This condition could occur due to excessive interference at rest or due to excessive centrifugal loading at maximum speed. Again, both temperature conditions are considered. If low cycle fatigue failure was a concern, constraints 36 to 39 could be replaced or supplemented by similar constraints placed on the circumferential stress.

The example design study undertaken had the numerical constraint data:

$$\sigma_{UCS,mag} = -500 \text{ MPa}$$

$$\sigma_{allow,sleeve} = 600 \text{ MPa}$$

$$T_{max} = T_{amb} + 200 \text{ °C}$$

$$\omega_{max} = 100 \text{ krpm}$$

The magnet had an inner radius of 6.35 mm and an outer radius of 11.35 mm. The radial interference at rest, $\delta_{\omega=0}$, and the outer radius of the sleeve, R_O, were treated as design variables with the ranges:

$$0 \leq \delta_{\omega=0} \leq 60 \text{ μm}$$

$$13 \leq R_O \leq 14.5 \text{ mm}$$

Figure 6 shows the circumferential stress at the inner radius of the magnet at rest and ambient temperature. The magnitude of this stress is limited by constraint 30 to be less than 500 MPa. This constraint boundary is indicated in the figure and the result non-feasible set of designs are hatched out. The stress magnitude increases as the interference

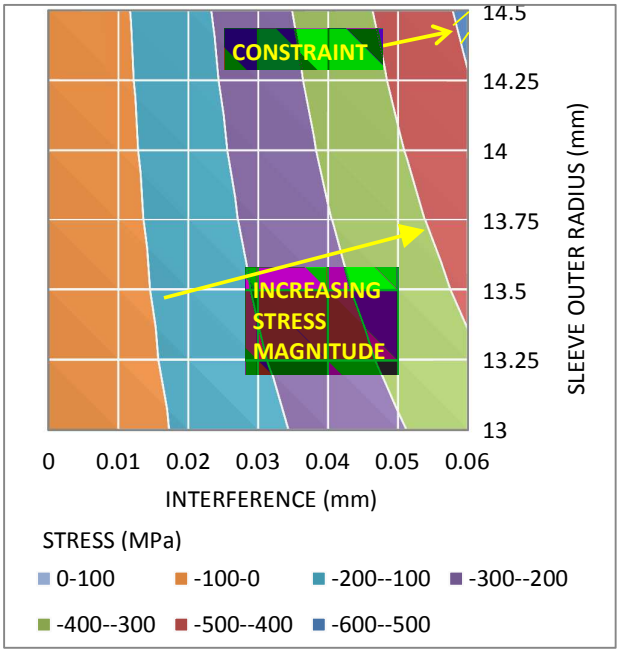

Fig. 6. $\sigma_{\theta ii}$ *at* $\omega = 0$ *for* $T = T_{amb}$

increases due to the increased compressive load on the magnet outer radius. This stress is also affected by the thickness of the sleeve with thicker and hence stiffer sleeves increasing the compressive load.

Increasing the temperature of the assembly causes the magnet and sleeve to expand. Since in this case, the coefficient of thermal expansion of the sleeve is greater than that of the magnet, the magnitude of stress due to interference at the inner radius of the magnet is reduced, as shown in figure 7. Indeed, for interference levels less than 0.01 microns the interference is lost as the components expand and no stress is generated.

Due to the low tensile strength of the magnet material, the circumferential stress must remain compressive. The value of this stress over the design space at both the outer

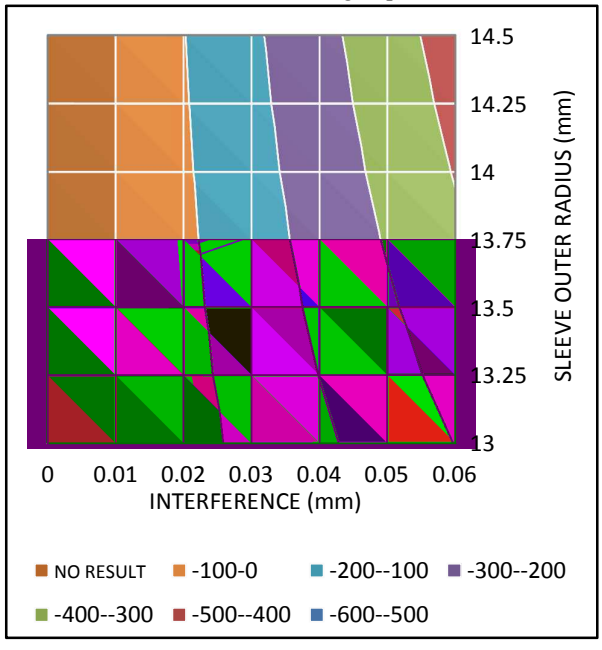

Fig. 7. $\sigma_{\theta ii}$ $at = 0$, $T = T_{max}$

diameter and bore of the magnet is shown in figures 8 and 9 at both ambient and maximum temperature. At both temperatures increasing interference and to a lesser extent, increasing sleeve thickness allows both constraints to be satisfied. At elevated temperature the degree of initial interference must be increased to compensate for the reduction in interference due to differential thermal expansion.

Within the sleeve the peak von Mises stress will be at the common radius. The variation of this stress over the design space at ambient and elevated temperature, at rest is shown in figure 10. The limiting condition, $\sigma_{VMco} \leq 600$ MPa is reached for larger levels of interference as the shrinkage pressure within the sleeve is increased. However, increasing the thickness of the sleeve reduces the stress. Again, stress is relaxed when thermal expansion occurs.

Figure 11 shows the von Mises stress at the bore of the sleeve at maximum speed. Comparing the results in this figure to those in figure 8, the stress is increased as speed is increased due to the addition of centripetal forces acting on the sleeve. This increase is small as during rotation the

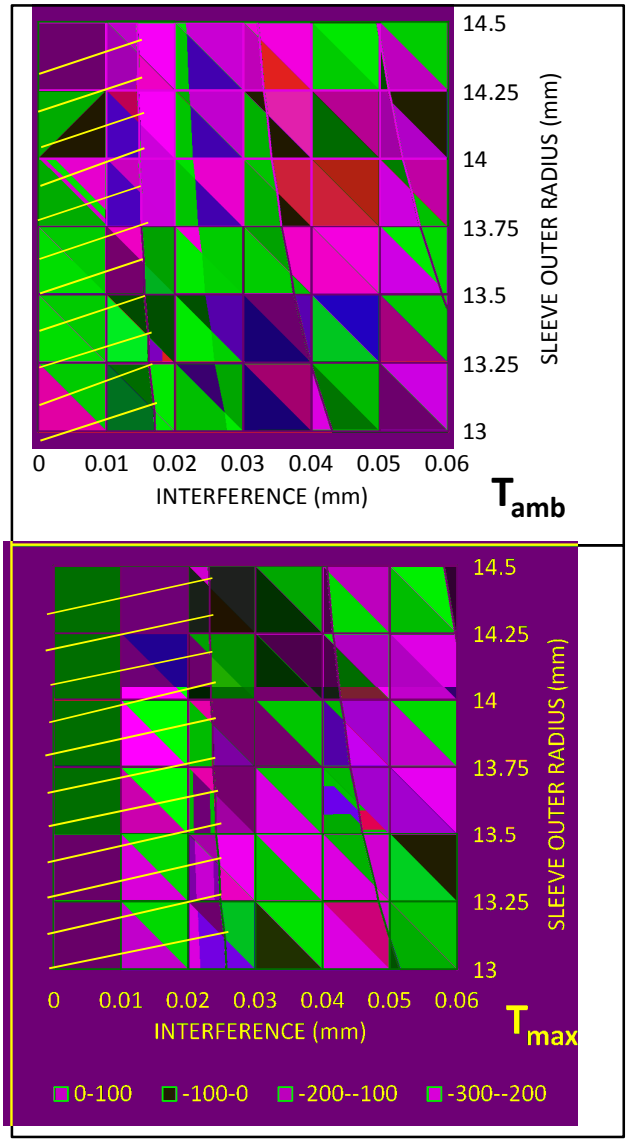

Fig. 8. $\sigma_{\theta ic}$ *at* $\omega = \omega_{max}$ $T = T_{amb}$ *and* T_{max}

differential expansion of the magnet and sleeve in this case reduces the degree of interference. However, an increased level of initial interference is required to keep the stress during rotation acceptable.

Examining the various constraints within the design space, the particular design being evaluated here is bounded by the circumferential stress at the common radius in the magnet at maximum speed and elevated temperature (figure 8) and the von Mises stress at maximum speed at the common radius in the sleeve at ambient temperature (figure 11). These constraints are the active constraints. Other constraints are inactive.

For a specified magnet diameter, the rotor assembly is optimized by minimizing the sleeve thickness. This reduced the virtual air gap between the stator and the rotor and also reduces the inertia of the rotor. Considering the active constraints in the study considered here, the optimum rotor design has a sleeve outer radius of 13 mm (i.e. the minimum thickness) and a radial interference between 0.026 and 0.036 mm. An increased range of radial interference is possible if the sleeve thickness is increased.

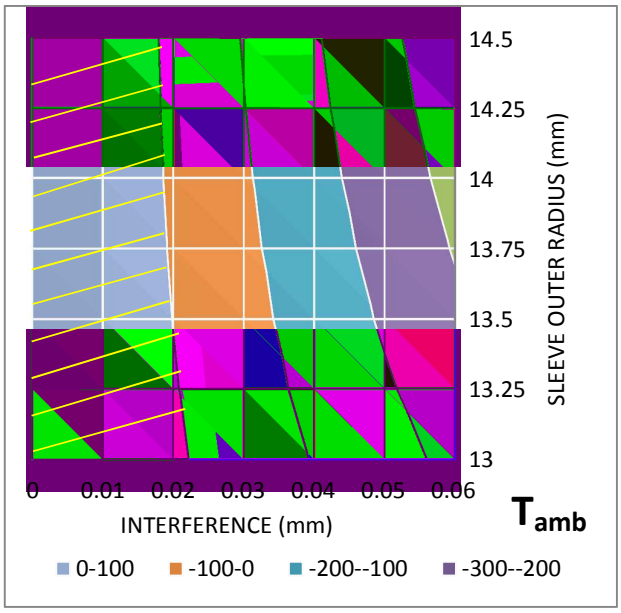

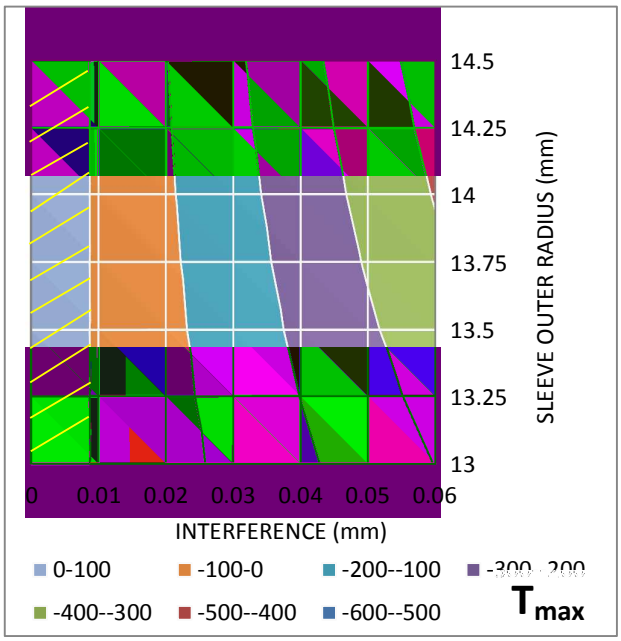

Fig. 9. $\sigma_{\theta ii}$ *At* $\omega = \omega_{max}$ *at* T_{amb} *and* T_{max}

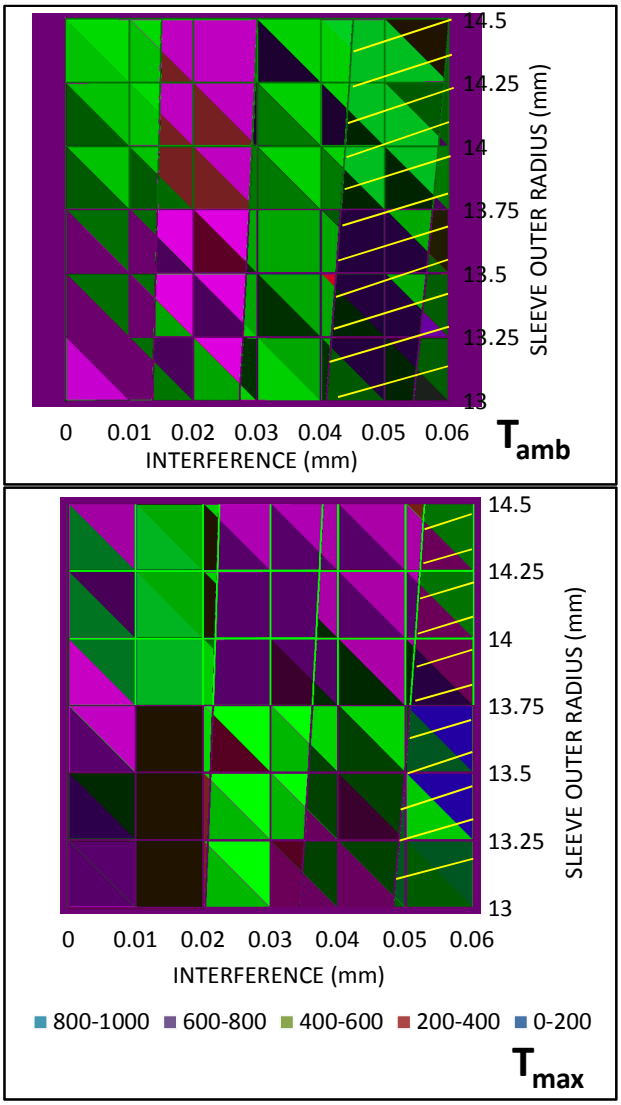

Fig. 10. σ_{VMoc} *at* $\omega = 0$ *at* T_{amb} *and* T_{max}

6. Conclusions

Current theoretical models available to model the stresses and strains in interfering, rotating cylinders do not account for load transfer due to friction in the axial direction. A new theoretical model has been derived which does account for the load transfer.

The new theoretical model shows very close agreement with a finite element model of a representative cylinder assembly away from the free ends of the assembly.

Finite element analysis has demonstrated that friction does prevent axial slip between the cylinders. The load transfer required to prevent this slip occurs towards the free end of the cylinders.

The new theoretical model allows the design space to be quickly explored without having to create numerical models. A feasible set of designs can be determined and the active constraints on that set identified.

The new theoretical model can be used to aid the selection of an optimum rotor design.

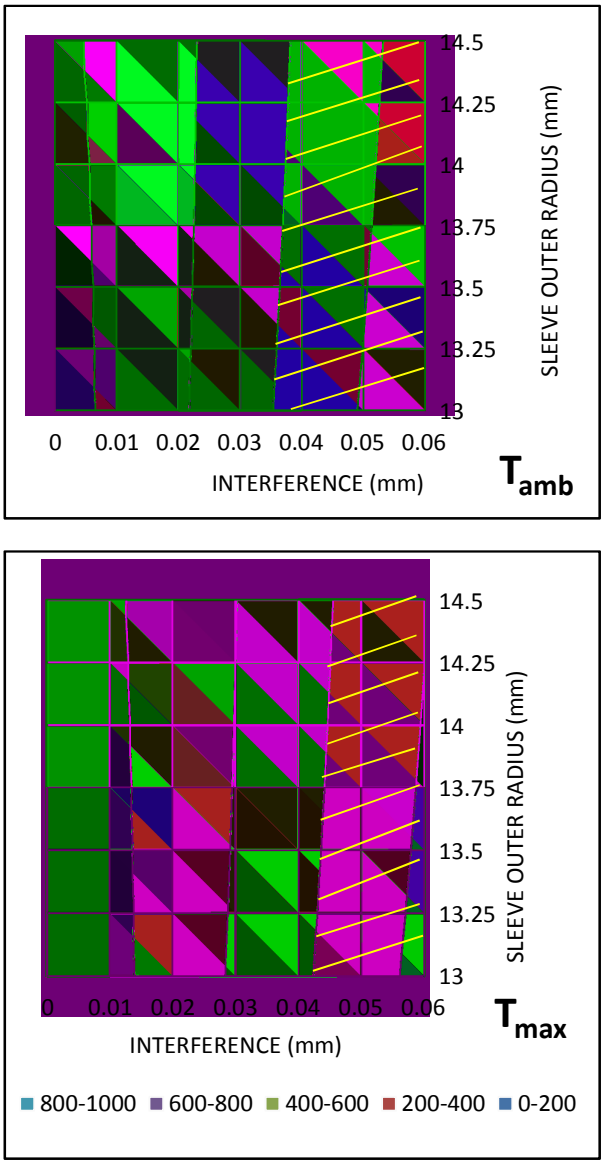

Fig. 11. σ_{VMoc} *at* $\omega = \omega_{max}$ *at* T_{amb} *and* T_{max}

7. Acknowledgments

The work described here has been funded by BorgWarner Turbo Systems and the Regional Growth Fund Grant Award 01.09.07.01/1789C

8. References

[1] Arsie, I., Cricchio, A,. Pianese, C., et al., A comprehensive powertrain model to evaluate the benefits of electric turbo compound (ETC) in reducing CO2 emissions from small Diesel passenger cars. 2014, SAE Technical Paper.
[2] Keller, R., E. Mese, and J. Maguire. Integrated system for electrical generation and boosting (iSGB). in Electrical Machines and Systems (ICEMS), 2014 17th International Conference on. 2014. IEEE.
[3] Gerada, D., High-Speed Electrical Machines: Technologies, Trends, and Developments. IEEE Transactions on Industrial Electronics, 2014. 61(6): p. 2946-2959.
[4] Binder, A., T. Schneider, and M. Klohr, Fixation of buried and surface-mounted magnets in high-speed permanent-magnet synchronous machines. Industry Applications, IEEE Transactions on, 2006. 42(4): p. 1031-1037.
[5] Kim, C.-K. and T.-H. Kim, Finite Element Analysis on the Strength Safety of a Hybrid Alarm Valve. Journal of manufacturing engineering & technology, 2012. 21(2): p. 221-224.
[6] Smith, D.J.B., Mecrow, B.C., Atkinson, G.J., et al., Shear stress concentrations in permanent magnet rotor sleeves. in Electrical Machines (ICEM), 2010 XIX International Conference on. 2010. IEEE.
[7] Gieras, J.F. Design of permanent magnet brushless motors for high speed applications. in Electrical Machines and Systems (ICEMS), 2014 17th International Conference on. 2014. IEEE.
[8] Zhang, J., Chen, W., Huang, X., et al., Evaluation of Applying Retaining Shield Rotor for High-Speed Interior Permanent Magnet Motors. IEEE TRANSACTIONS ON MAGNETICS, 2015. 51(3): p. 8100404.
[9] Varaticeanu, B.D., P. Minciunescu, and D. Fodorean, Mechanical Design and Analysis of a Permanent Magnet Rotors used in High-Speed Synchronous Motor. Electrotehnica, Electronica, Automatica, 2014. 62(1): p. 9.
[10] Tenconi, A., S. Vaschetto, and A. Vigliani, Electrical Machines for High-Speed Applications: Design Considerations and Tradeoffs. IEEE Transactions on Industrial Electronics, 2014. 61(6): p. 3022-3029.
[11] Abdollahi, S., M. Mirzaei, and H. Lesani. Rotor optimization of a segmented reluctance synchronous motor utilizing genetic algorithm. in Electrical Machines and Systems, 2009. ICEMS 2009. International Conference on. 2009. IEEE.
[12] Danilevich, J.B., Kruchinina, I.Y., Antipov, V.N., et al., Some problems of the high-speed permanent magnet miniturbogenerators development. in ICEM 2008. 18th International Conference on Electrical Machines. 2008. IEEE.
[13] Kim, S.-I., Kim, Y-K., Lee, G-H., et al., A novel rotor configuration and experimental verification of interior PM synchronous motor for high-speed applications. Magnetics, IEEE Transactions on, 2012. 48(2): p. 843-846.
[14] Smith, J.S. and A.P. Watson. Design, manufacture, and testing of a high speed 10 MW permanent magnet motor and discussion of potential applications. in Proceedings of the Thirty-Fifth Turbomachinery Symposium. 2006.
[15] Wang, T., Wang, F., Bai, H., et al., Optimization design of rotor structure for high speed permanent magnet machines. in Electrical Machines and Systems, 2007. ICEMS. International Conference on. 2007. IEEE.
[16] Solecki, R., and Conant, R.J., Advanced mechanics of materials. 2003, New York: Oxford University Press.
[17] Zhang, F., Du, G., Wang, T., et al., Rotor Retaining Sleeve Design for a 1.12-MW High-Speed PM Machine. IEEE Transactions on Industry Applications, 2015. 51(5): p. 3675-3685.
[18] Borisavljevic, A., H. Polinder, and B. Ferreira. Overcoming limits of high-speed PM machines. in 2008 18th International Conference on Electrical Machines. 2008.

[19] Yon, J.M., Mellor, P.H., Wrobel, R., et al., Analysis of semipermeable containment sleeve technology for high-speed permanent magnet machines. Energy Conversion, IEEE Transactions on, 2012. 27(3): p. 646-653.
[20] Li, W., Qiu, H., Zhang, X., et al., Analyses on Electromagnetic and Temperature Fields of Superhigh-Speed Permanent-Magnet Generator With Different Sleeve Materials. IEEE Transactions on Industrial Electronics, 2014. 61(6): p. 3056-3063.